Femtosecond single-beam direct laser poling of stable and efficient second-order nonlinear optical properties in glass

Gautier Papon, Nicolas Marquestaut, Yannick Petit, Arnaud Royon, Marc Dussauze, Vincent Rodriguez, Thierry Cardinal, Lionel Canioni

Femtosecond single-beam direct laser poling of stable and efficient second-order nonlinear optical properties in glass

G. Papon,[1] N. Marquestaut,[1] Y. Petit,[1,2,a)] A. Royon,[1] M. Dussauze,[3] V. Rodriguez,[3] T. Cardinal,[2] and L. Canioni[1]
[1]*Univ. Bordeaux, LOMA, UMR 5798, F-33400 Talence, France and CNRS, LOMA, UMR 5798, F-33400 Talence, France*
[2]*CNRS, ICMCB, UPR 9048, F-33608 Pessac, France and Univ. Bordeaux, ICMCB, UPR 9048, F-33400 Pessac, France*
[3]*Univ. Bordeaux, ISM, UMR 5255, F-33400 Talence, France and CNRS, ISM, UMR 5255, F-33400 Talence, France*

We depict a new approach for the localized creation in three dimensions (3D) of a highly demanded nonlinear optical function for integrated optics, namely second harmonic generation. We report on the nonlinear optical characteristics induced by single-beam femtosecond direct laser writing in a tailored silver-containing phosphate glass. The original spatial distribution of the nonlinear pattern, composed of four lines after one single laser writing translation, is observed and modeled with success, demonstrating the electric field induced origin of the second harmonic generation. These efficient second-order nonlinear structures (with $\chi^{(2)}_{eff} \sim 0.6\,\mathrm{pm\ V^{-1}}$) with sub-micron scale are impressively stable under thermal constraint up to glass transition temperature, which makes them very promising for new photonic applications, especially when 3D nonlinear architectures are desired.

I. INTRODUCTION

Second-order nonlinear optical function is broadly demanded for a large application panel as the creation of new and intense coherent radiations through parametric frequency conversion,[1] nonlinear integrated optics based on electro-optical effects,[2] sub-wavelength laser beam metrology,[3] nonlinear metamaterial engineering,[4] or *in vivo* biological imaging with optimized nonlinear tags.[5] The access to such property compatible with micro-photonic devices is still highly challenging and various approaches co-exist. On the one hand, organic crystals are very promising for optical circuit engineering but they still suffer from low optical damage thresholds. On the other hand, inorganic non-centrosymmetric crystals have been widely exploited even if they are more compatible with bulk devices, taking into account intrinsic cost and time limitations for the growth of very large volumes. For integrated optics, crystalline film technology has been developed but, as for the bulk materials, it suffers from expensive and time-consuming processes. Regarding the vitroceramics, the localized creation of micro- or nano-crystallites in a glassy matrix is a nontrivial approach, since it requires both the control of the crystallite orientation and its three-dimensional (3D) spatial distribution,[6] without affecting transmission properties with unwanted diffusion aspects. Even if frequency-doubling metallic nanoparticles may be well oriented, they are frequently limited to surface thin films with significant surface plasmon resonance induced losses.[7] Thermal poling of glasses gives access to electric field induced second harmonic generation (EFISHG), but such approach is limited to 2D surface structuring and the patterning shape and dimensions are constrained by that of the applied electrodes.[8–13]

However, laser-assisted processes have led to significant achievements to produce second harmonic generation (SHG), due to the local inversion symmetry breaking, related to the creation of a spatially modulated static electric field distribution. This was initially obtained in fibers by co-propagating a fundamental laser beam and its second-harmonic in the nanosecond regime. The four-wave mixing of these light fields gives rise to a periodically alternated static electric field.[14] This was even enhanced by co-propagating such two beams with an additional UV light, from either a CW source[15] or the third-harmonic radiation.[16] The EFISHG efficiency and stability were shown to be highly dependent on the considered glass matrix, related to the nature of the laser-induced defects.[17] Other works on photosensitized silver-doped silicate or phosphate glasses addressed the space-selective precipitation of nanoparticles,[18,19] without, however, accessing the EFISHG process in these cases.

In this article, we propose a new approach based on single-beam fs direct laser writing (DLW), to create on demand an efficient and stable SHG functionality, with a sub-micron control of its 3D spatial distribution and orientation, whose process is fully compatible with both local micro-integrated optics and large-scale 3D SHG architecture. We have developed a tailored silver-containing phosphate glass, which allows fast-access and cost-limited large samples with excellent optical quality. Under femtosecond (fs) direct laser writing, such glass provides very strong optical contrast in fluorescence[20] or third-order nonlinear optical property (third harmonic generation),[21] compatible with

a)Author to whom correspondence should be addressed. Electronic mail: yannick.petit@u-bordeaux1.fr

multi-level 3D high-density data storage.[21,22] We report on the fact that single-beam fs DLW can also generate a localized SHG response, which significantly extends previous studies.[23] We demonstrate that the laser-induced nonlinear function provides an efficient and remarkably stable optical brick for further nonlinear photonics applications, such as integrated nonlinear frequency converters or electro-optics devices. Such original approach shows the ability to perform fs direct laser poling (DLP), by obtaining an EFISHG behavior with efficiencies (of the order of 0.6 pm V^{-1} as long as thermal constraints remain below glass transition temperature), similar to that obtained by thermal poling. Therefore, DLP opens exciting potentialities, with a direct and versatile access to 3D nonlinear functionalized materials.

II. EXPERIMENTAL METHOD

A. Glass sample, DLW setup, and irradiation protocol

The considered glass sample was a tailored silver and zinc phosphate glass (labeled PZA), annealed, cut with a typical thickness of 1 mm, and polished to optical quality,[24] with a 5% Ag_2O concentration (in mol. %). The experimental DLW setup was based on a home-made nonlinear microscope as described elsewhere,[25] including a fs laser (KGW:Yb oscillator, 6 W, 10 MHz, 470 fs at 1030 nm, T-Pulse 500, Amplitude Systemes), an acousto-optic modulator to control the irradiation parameters as the irradiation duration and the transmitted irradiance, a microscope objective (Mitutoyo, APO PLAN NIR, 100×, NA 0.7), and a high precision 3D translation stage for nanometric positioning and displacement of the glass sample under irradiation (XMS-50 stages, Micro-Contrôle, 20 nm resolution).

DLW was performed by linearly moving the glass sample at controlled speeds from 20 up to 300 μm s^{-1} locally corresponding typically to 1.0×10^6 down to 0.66×10^5 pulse numbers, for different fluencies from 3.52 to 5.15 J cm^{-2} (from 7.5 to 11.0 TW cm^{-2}). DLW-induced linear structures were processed, with lengths of 100 μm, and located in a plane typically at 170 μm below the glass surface, which prevents any interaction between the localized structured volume and the glass surface. This eliminates any possible physico-chemistry at the surface with the surrounding atmosphere, which makes the SHG independent from surface effects. The linear polarization of the writing beam was parallel to the sample translations (and thus to the lines) during the DLW process.

B. Nonlinear SHG imaging setup

The experimental nonlinear imaging setup was based on a second home-made nonlinear microscope including a fs laser (KGW:Yb oscillator, 1 W, 50 MHz, typically 200 fs at 1030 nm, T-Pulse 20, Amplitude Systemes), a half-wave plate before a Faraday rotator to isolate the laser from beam reflection and to control the irradiance of the laser pulses, an adapted pair of GTI (Gires-Tournois interferometer) mirrors to compensate the Faraday rotator group velocity dispersion, a polarization filter, a loosely focusing objective preventing significant longitudinal polarization at the focus (Olympus, 10×, NA 0.25) followed by a sharp collecting objective (Olympus, 100×, NA 0.8), a polarization analyzer and a spectral bandpass filter centered at 515 nm for the analysis of the SHG signal and, finally, a Peltier-cooled high-sensitivity CCD camera (Hamamatsu C4742-95), as seen in Fig. 1. The sample position between the two objectives was adjusted with a high precision 2D translation stage in the horizontal plane (Newport, SMC100) and with a manual micro-precision controlled for longitudinal displacement. Second harmonic signal was obtained by numerically integrating the pixels of the images of the nonlinear emitting patterns, once these images were properly conjugated and obtained on the CCD camera. The fundamental and second-harmonic radiation spectra have been controlled with a fiber spectrometer.

III. RESULTS AND DISCUSSION OF THE EFISHG RESPONSE

A. Dependence with the incident laser power

The nonlinear response of the laser-induced linear structures was studied with the nonlinear SHG setup on an individual linear structure that resulted from a single and unique displacement of the sample at constant speed. Fig. 2(a) shows the image of the illuminated part of an individual linear structure, generating a coherent second harmonic signal associated to a non-trivial spatial pattern made of four distinct lines, as deeply analyzed and modeled in Secs. III C and

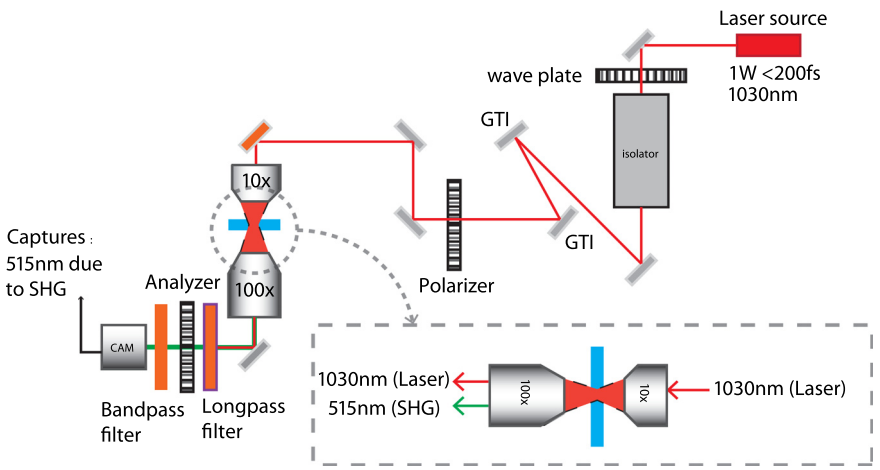

FIG. 1. Experimental setup for nonlinear SHG microscopy imaging after direct laser poling.

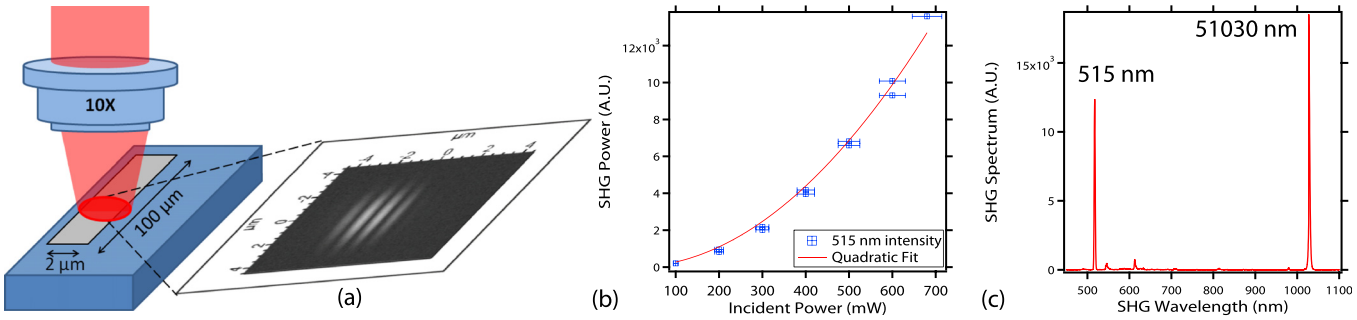

FIG. 2. (a) Coherent image of the second harmonic response at 515 nm, under 1030 nm weakly focused probe beam on a 100 μm long individual laser-induced poled linear structure, associated to a non-trivial spatial pattern made of four sub-micron distinct lines. (b) Quadratic dependence of the second harmonic signal at 515 nm obtained by numerical integration of the imaged pattern. (c) Simultaneous recording of the fundamental and second-harmonic spectra.

III E. Due to the incident laser focusing with the 10× objective, only a short part of about 4 μm is illuminated among the 100 μm long structure. Therefore, the observed SHG signal amplitude results from both the spatial distribution of the nonlinear structure and the illuminating Gaussian beam transverse profile. A spectral collection showed a very narrow peak at 515 nm, exactly half of the incident laser wavelength, demonstrating a nonlinear frequency-doubling process (Fig. 2(c)). Moreover, a power scan of the incident laser led to a clear quadratic dependence of the SHG amplitude, as seen in Fig. 2(b) after the numerical integration of the whole pictures collected by the high-sensitivity camera, in agreement with an effective second-order nonlinear interaction. Despite its non-trivial spatial distribution of the SHG pattern, one should note that each emitting point of the linear structure undergoes quadratic power dependence. Such laser-induced nonlinear structures showed the same SHG signature all along the laser-written lines.

B. Dependence with the incident laser polarization or the collection polarization

The EFISHG response results from the effective coupling of a buried electric field with the nonlinear third-rank susceptibility tensor $\chi^{(3)}$. In the case of amorphous glasses, as for the cubic symmetry, among the $3^4 = 81$ $\chi^{(3)}_{ijkl}$ elements (indices i, j, k, l can be x, y, or z in the experimental frame), only $\chi^{(3)}_{iiii} = \chi^{(3)}_{jjjj}$ and $\chi^{(3)}_{iijj} = \chi^{(3)}_{ijij} = \chi^{(3)}_{ijji}$ are nonzero, where Kleinman symmetry adds the following relation $\chi^{(3)}_{iiii} = \chi^{(3)}_{iijj} + \chi^{(3)}_{ijij} + \chi^{(3)}_{ijji}$ with $i \neq j$, leading to $\chi^{(3)}_{iiii} = 3\chi^{(3)}_{iijj}$ in the case of purely electronic nonlinear response.[26] From a spectral point of view, $\chi^{(3)}_{ijkl}$ elements correspond to $\chi^{(3)}_{ijkl}(2\omega;\omega,\omega,0)$, where ω is the fundamental laser angular frequency, while the static electric field associated to the buried electric field corresponds to a null optical frequency.

We performed the analysis of the second harmonic intensity with respect to the transverse polarization orientation of the incident transverse laser field that propagated along the z-axis. Such polarization direction defines the arbitrary x-axis in the glass sample. The electric field E_{DC} decomposes in $\{E_{DC}.\cos(\theta), E_{DC}.\sin(\theta)\}$ along the $\{x, y\}$ axes in the plane perpendicular to the laser propagation direction, and where θ is the angle between the laser polarization and the static field. In such conditions, the second harmonic intensity writes as

$$I_{2\omega}(\theta) \propto \left|\chi^{(3)}_{yxxy}\right|^2 \left|E_{DC}\right|^2 I_\omega^2 \left\{9\cos^2(\theta) + \sin^2(\theta)\right\}. \quad (1)$$

We also performed the polarization analysis of the second harmonic emission, for the incident laser polarization fixed parallel to the static electric field direction labeled as the x-axis, with $\theta = 0$. In this case, for the angle β between the orientation of polarization analyzer and the static field direction, the polarized second harmonic intensity writes as

$$I_{2\omega}(\beta;\theta=0) \propto \left|\chi^{(3)}_{yxxy}\right|^2 \left|E_{DC}\right|^2 I_\omega^2 \left\{9\cos^4(\beta) + \sin^4(\beta)\right\}. \quad (2)$$

Figure 3 shows the SHG intensity with respect to the laser polarization orientation, in excellent agreement with Eq. (1). It confirms that we deal with an EFISHG process, with an effective nonlinear response $\chi^{(2)}_{eff} = 3\chi^{(3)} \bullet E_{DC}$, where • stands for the contracted product. In addition, it also shows that the orientation of the static electric field is perpendicular to the linear structure, since $\theta = 0$ is fixed here for the laser polarization perpendicular to the structure. On the other hand, we also verified that the dependence of the polarized second harmonic intensity, with respect to the linear collection orientation laser polarization orientation β, is in excellent agreement with Eq. (2). This confirms the optimal polarized collection along the static electric field orientation, for $\beta = 0$, while the laser polarization is perpendicular to the DLW-induced structure. Each second harmonic emitting point follows the same polarization dependence, except that each position is affected to a modulated efficiency that directly corresponds to the spatial distribution of the buried static electric field amplitude.

C. Dependence with the imaging focus depth and modeling of the EFISHG topology

The linear laser-induced poled structure, associated to a non-trivial pattern composed of four emitting lines, as seen in Fig. 2(a), has been studied in detail. In order to demonstrate the physical existence of this SHG spatial distribution and to ensure that no diffraction effect was at the origin of such unexpected observation, the incident probe laser polarization was set perpendicular to the linear structure, thus parallel to the static electric field direction, to solicit the largest effective second harmonic response with no analyzer.

Different coherent second harmonic images were collected for different depths of focusing by longitudinally

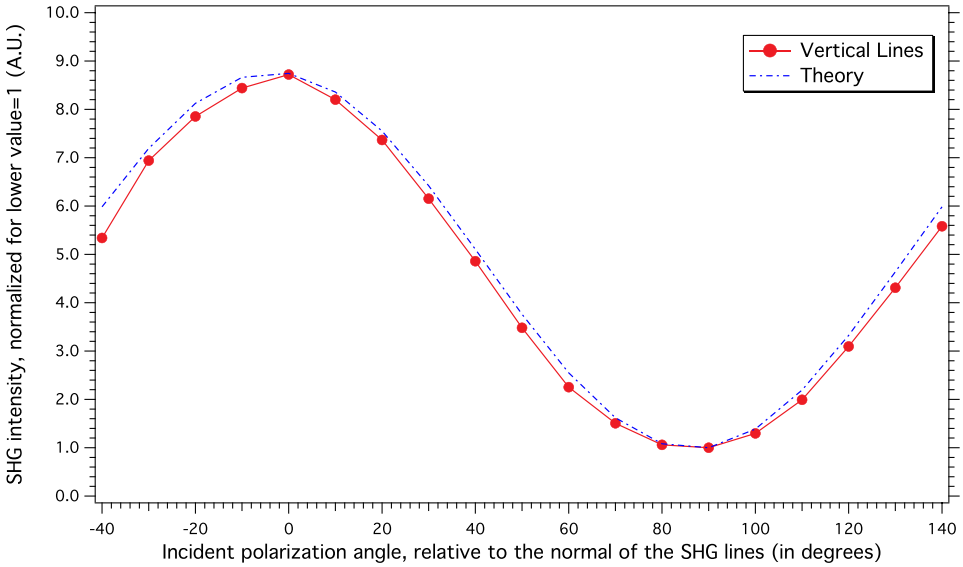

FIG. 3. Normalized EFISHG intensity versus the angle θ between the laser polarization orientation and the buried electric field. The EFISHG intensity was obtained from the whole integration of the related collected images, for which the associated modeling is in agreement with Eq. (1).

translating the position of the structured sample between the two illuminating and collecting objectives. Each of these two objectives had been set at fixed positions to optimize the collected second harmonic amplitude, which corresponds to the collection focal plane being overlapped with the illuminating focal plane. The optimized sample position, which provided the most intense second harmonic response, was labelled the "$Z=0$" sample position. Different images were recorded for sample positions at $Z=0$, 2, 4, and 8 μm, and the related transverse profiles were obtained by vertical integration along the linear structure direction of the images, as shown in Fig. 5. The second harmonic transverse profiles show (i) an intensity decay for sample positions away from the "$Z=0$" position, but most strikingly (ii) a strong profile reshaping and modification due to Fresnel diffraction introduced by the change of propagation distances of each second harmonic emitting point towards each position of the collection focal plane (being conjugated to the CCD camera). Therefore, we developed a model to simultaneously match the observations for all the different sample Z-positions by adjusting the static electric field transverse distribution while considering an invariant longitudinal distribution along the depth of the EFISHG structure (typically along 8 μm, corresponding to the nonlinear Rayleigh length of the DLW interaction). Since both second harmonic polarization components are proportional one to the other, the considered scalar model was sufficient to properly deal with the static electric field distribution and the subsequent EFISHG signal under weakly focused probe laser (objective 10×, NA 0.25). Indeed, such weak focusing prevents from depolarization of the incident beam at the focus, which avoids longitudinal solicitation of tensor components. For each EFISHG emitting point towards each collection point, the second harmonic optical field profile was described as

$$E_{2\omega}(X,Z) \propto \iint \frac{e^{i\left(k_{2\omega}.\sqrt{(X-x')^2+(Z-z')^2}+2k_{\omega}.z'+2.\mathrm{atan}(z'/Z_R)\right)}}{\sqrt{(X-x')^2+(Z-z')^2}} \times E_{\omega}^2(x',z').P(x',z')dx'dz', \quad (3)$$

where (x', z') and (X, Z) variables correspond to the Cartesian coordinates of the considered emitting point of the nonlinear structure and to those of the considered collection point for a given sample position, respectively; k_ω is the incident laser probe wave vector, collinear to the Z propagation direction; Z_R is the Rayleigh length, and the related Gouy phase shift $\mathrm{atan}(z'/Z_R)$ accounts twice in the phase term since the second harmonic field is proportional to the square of the incident laser field; $k_{2\omega}$ is the wave vector of each second harmonic emitting point; $E_\omega(x', z')$ stands for the spatial distribution of the incident probe beam, and $P(x', z')$ for the second harmonic signal amplitude that derives from the static electric field spatial distribution. The calculated second harmonic intensity at each collection point was obtained by the integration of the second harmonic waves coherently emitted from each point of the EFISHG structure, taking into account the interferences of all the generated waves at 515 nm and the associated dephasing.

Figure 4 reports on the experimental and calculated results at optimal focusing, for the sample position at $Z=0$ μm. Fig. 4(a) shows the experimental EFISHG profile resulting from the convolution of the transverse profile of the probe laser beam squared intensity with a laser-induced poled linear structure. Such pattern is composed of four lines, as a direct consequence of the persistent buried electric field distribution, as also further demonstrated in Fig. 5 after fitting with our model from Eq. (3). Fig. 4(b) depicts the calculated EFISHG spatial distribution, including (i) the optimal modeling of the static field spatial distribution, (ii) the relative sign of the buried electric field (which corresponds to its orientation changes), and (iii) the influence of the Gaussian intensity shape of the laser beam. Further investigations should provide the true sharpness of the spatial modulations of the buried electric field, since our data show roughly 350 nm lateral resolution (FWHM), which is typically that of the collection setup.

Figure 5 significantly extends Fig. 4 to all the different sample positions that were simultaneously considered for optimal adjustment of the buried electric field distribution. Fig. 5 shows the excellent agreement of the model with the experimental data. Such SHG-emitting structure typically corresponds to the nonlinear excitation of double Young slits

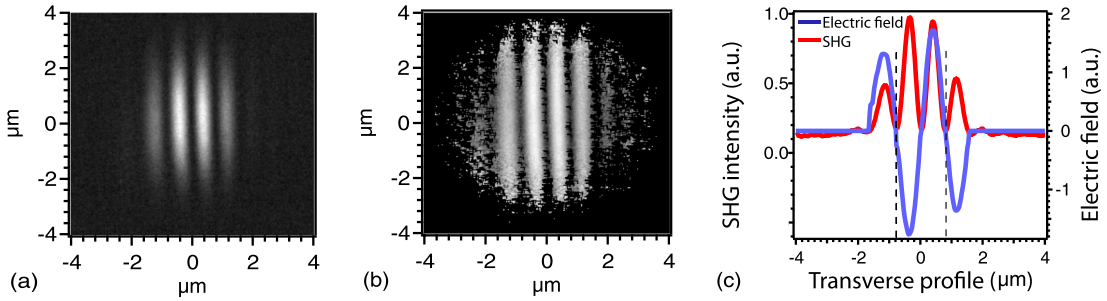

FIG. 4. (a) Experimental EFISHG profile resulting from the convolution of the incident probe laser beam transverse intensity profile with a laser-induced poled linear structure. Note that such pattern is composed of 4 lines, as a direct consequence of the persistent buried electric field distribution. (b) Calculated EFISHG response, including the static electric field distribution from optimization of our simulation model to match the experimental data, but also the relative sign of such buried field, as well as the Gaussian beam intensity profile. (c) Projection of both the experimental EFISHG profile and the associated electric field calculated distribution.

with π-dephasing, leading to an exactly null intensity in the center, as observed in Fig. 4 for any imaging depth. This demonstrates the opposite direction of the buried static field with inversion symmetry with respect to the center of the laser beam, as also depicted in Fig. 4(c), which is in agreement with the recently accepted paper in which the spatial correlation between fluorescence and EFISHG spatial distributions is detailed.[27] This also demonstrates the topology of the EFISHG pattern and the true physical existence of the four lines that result from one single DLW linear translation. Indeed, the intensity maxima are well positioned and the relative intensities are well described, even for large sample displacement up to $Z = 8\ \mu$m. Moreover, it is remarkable that each of the four individual lines of the EFISHG pattern shows typical 350 nm width (FWHM), well below the diffraction limit of the used laser at 1030 nm during DLP. Such width results from both the coherent construction of the second harmonic field and the diffraction-limited resolution of the collecting objective (100×, NA 0.8).

D. Dependence with the DLW parameters

The DLW parameters only affect the EFISHG amplitude. On the contrary, both the EFISHG spatial distribution and its polarization dependences at the excitation and collection remained almost unmodified. As described in the irradiation protocol in Sec. II A, up to 8 translation speeds (20, 60, 110, 140, 180, 220, 260, and 300 μm s^{-1}) were tested during DLW for four distinct fluencies (3.52, 3.99, 4.53, and 5.15 J cm^{-2}), typically corresponding to the overlapped irradiation of 10^6, 3.3×10^5, 1.8×10^5, 1.4×10^5, 1.1×10^5, 0.9×10^5, 0.75×10^5, and 0.66×10^5 pulses at each position along the linear structures.

Figure 6 shows the relative amplitude of the integrated EFISHG signal versus the DLW parameters, and demonstrates the rather independent influence of the writing speed for such nonlinear response. On the contrary, the irradiance influence is clear, with an original threshold and plateau behavior. Indeed, a EFISHG response appears for quite a limited incident fluence as low as 3.52 J cm^{-2} (7.5 TW cm^{-2}), while a saturation of the EFISHG amplitude is rapidly observed from moderate irradiation at 3.99 J cm^{-2} (8.5 TW cm^{-2}).

Another striking aspect is that the observed EFISHG depends on the DLW parameters in a different manner compared to the induced material modification. Indeed, laser-induced fluorescence is related to the creation and growth of silver clusters, which was showed to increase logarithmically with the number of pulses,[23] while we report here the independence of the second harmonic signal with the translation speed, which corresponds to the very fast saturation of the EFISHG response with the incident local number of pulses. Moreover, at 3.52 J cm^{-2}, we report on significant EFISHG while no fluorescence could be measured at that stage. Such crucial observation demonstrates a remarkable point, namely that the buried electric field is created at early stage from the first laser pulses, especially prior to the silver cluster formation.

These observations provide a significant breakthrough in the understanding of the writing processes in these tailored glasses with femtosecond lasers. We previously thought that the DLW of distinct silver clusters, associated to ion and silver metal diffusion motions, was leading to the creation of a net stabilized space charge separation at the root of the second harmonic response.[24] Actually, we demonstrate here that the static electric field appears in an independent process to that of the creation of the fluorescent silver species. Correlative fluorescence and second harmonic microscopy were recently reported in detail elsewhere,[27] where we demonstrated that both the buried space charge separation and its related electric potential modulation are at the root of the chemical growth and stabilization of the fluorescent silver clusters. These findings, about the electric potential modulations and subsequent silver cluster stability and about the initial glassy matrix reductive/oxidative potentials, should further be discussed and compared with the cases of gamma or ion irradiations.[28]

Finally, the microscopic origin of the static electric field and its stabilization still remain an open question, beyond the scope of this article. However, we can mention that other studies are in progress in order to correlate the modifications of the cationic concentrations, evidencing changes in the Ag^+ spatial distribution, with the laser-induced creation of the second-order nonlinear response. Therefore, we believe that each laser pulse generates free electrons that get trapped at the periphery of the beam focused spot. Such fast dynamics of the electrons is then followed by a slow pulse-after--pulse build-up of the EFISHG response in correlation with cationic motions, especially that of Ag^+ ions. Besides, the stabilization of such a static electric field is most likely to be

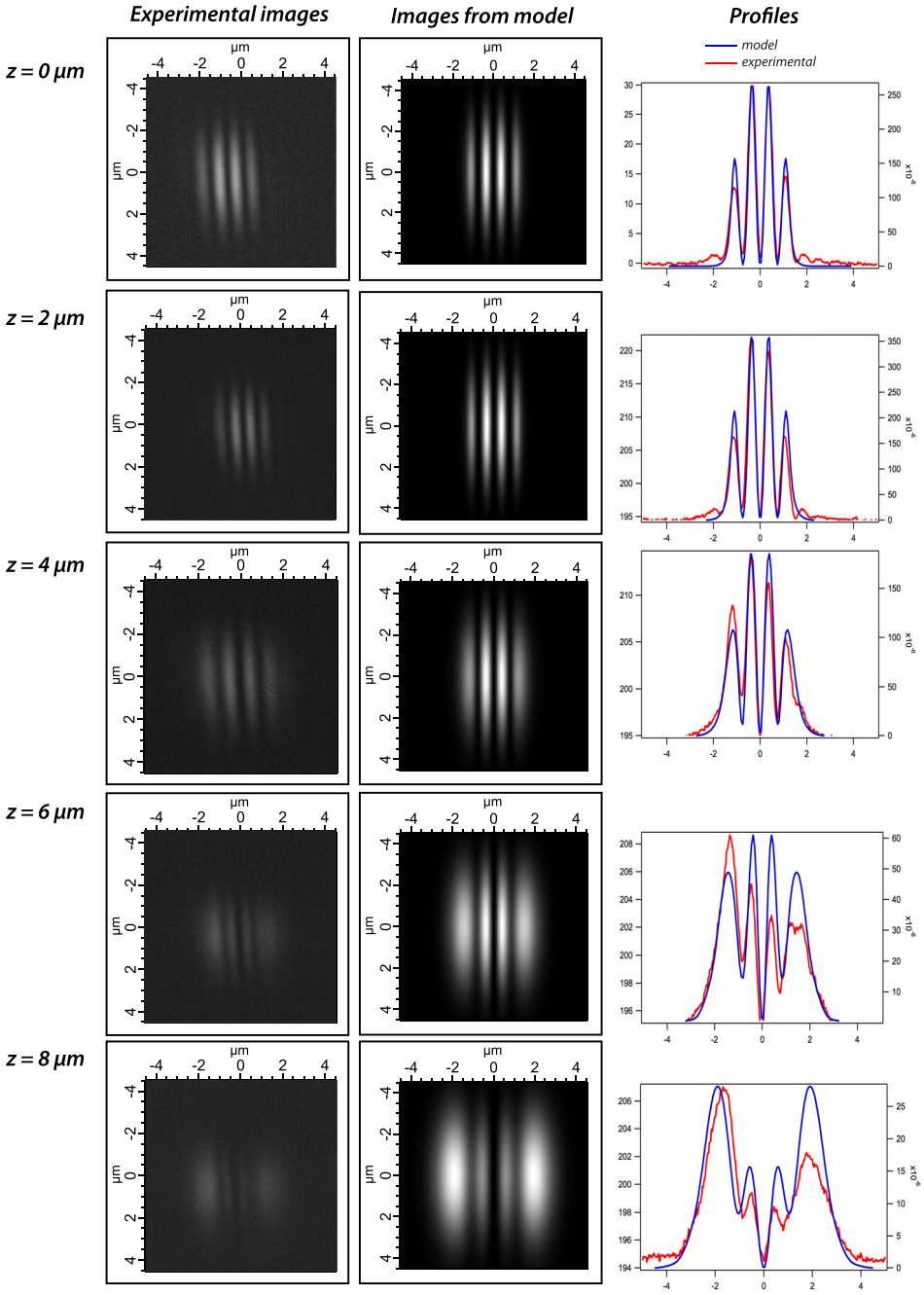

FIG. 5. Coherent EFISHG images recorded with a 100×, NA 0.8 objective, for different sample positions Z = 0, 2, 4, and 8 μm, respectively. Calculated SHG response after optimal adjustment of the topology of the buried electric field distribution. Associated experimental and calculated EFISHG profiles showing excellent agreement and demonstrating the physical existence of the EFISHG pattern with 4 lines.

associated to charge compensation as well as creation and motion of other species.

E. Efficiency and stability of the EFISHG structures

The efficiency of our frequency-doubling structures was estimated by comparing the EFISHG signal of the studied laser-poled glass with that of a reference thermally poled borophosphate niobium (BPN) glass (with 42 mol. % Nb_2O_5). Such BPN sample exhibits large EFISHG efficiencies up to $\chi^{(2)}_{\text{eff}} \sim 2\,\text{pm V}^{-1}$, with a poled zone (thickness $h_{\text{BPN}} = 4.2\ \mu$m) below the surface.[12,29] In the BPN glass, the buried electric field shows a homogeneous spatial distribution with its direction perpendicular to the surface. Therefore, we introduced a liquid crystal polarization plate (Arcoptics) in the nonlinear SHG microscope to get a NIR fs radially polarized probe beam. After focusing at the glass surface, we obtained a mostly longitudinally polarized beam that led to the optimal probing of the BPN nonlinear response by predominantly collecting the solicited $\chi^{(2)}_{xzz}$ effective coefficient.

EFISHG signals were carefully rescaled to provide relevant comparison between intrinsic efficiencies of both laser-poled phosphate glass and thermally poled BPN glass. First, signals were rescaled with experimental settings such as the incident probe laser power and the camera detection acquisition time. Second, the coherence lengths in each glass were considered. In the case of the studied phosphate glass, the poled zone is simulated to show a thickness of $h_{\text{PZA}} = 8\ \mu$m, which is also comparable with its coherence length $l_c = 8.58\ \mu$m ($n_\omega = 1.595$ at 1.03 μm and $n_{2\omega} = 1.605$ at 0.515 μm). In the BPN glass, the coherence length $l_c = 3.68\ \mu$m (with $n_\omega = 1.79$ and $n_{2\omega} = 1.86$) is also comparable to the 4.2 μm thick

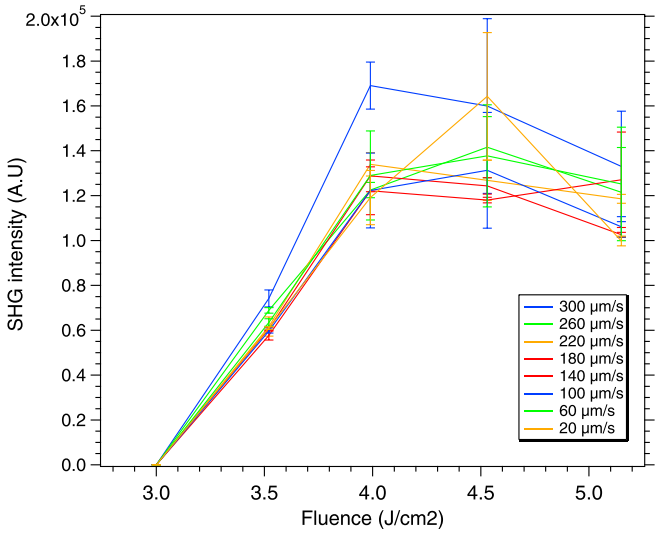

FIG. 6. EFISHG intensity (in arbitrary units) versus the incident DLW fluencies, for different cumulated pulse number corresponding to various glass sample translation speeds, showing (i) a quite invariance of the EFISHG signal with the cumulated number of pulses, and (ii) a DLW threshold for writing and a subsequent remarkably surprising saturation of the EFISHG response for fluencies above 4 J cm^{-2}, typically corresponding to 8.5 TW cm^{-2}.

thermally poled zone. In each glass, the poled zone typically shows the same depth as the related coherence length, ensuring that there were no successive constructive and destructive interferences in the SHG signal build-up. Such precaution ensures that each measured EFISHG signal is relevant of each solicited effective coefficient in both glasses. Third, since our nonlinear four-line pattern exhibits transverse dimensions smaller than the section $S_{PZA}^{IR\,beam}$ of the focused IR beam, we also considered the active ratio $\alpha_{PZN} = S_{PZA}^{structures}/S_{PZA}^{IR\,beam}$ of the illuminated section $S_{PZA}^{structures}$ that contributes to the SHG response, estimated at $\alpha_{PZN} \sim 10\%$. Since the BPN sample shows a poled surface with a homogeneous transverse profile, its active ratio $\alpha_{BPN} = S_{BPN}^{poling}/S_{BPN}^{IR\,beam}$ equals unity, exactly. The section $S_{BPN}^{IR\,beam}$ was considered similar to the $S_{PZA}^{IR\,beam}$ section. Therefore, we calculated the ratio of the effective second-order susceptibility of our PZA glass and the BPN reference sample, including the experimental measurements and the numerical integration of the propagation equations through the active nonlinear structures,[26] as following:

$$\frac{\chi^{(2)}_{eff\,xxx}[PZA]}{\chi^{(2)}_{eff\,xzz}[ref]} = \sqrt{\frac{T_{2\omega,ref}\,T^2_{\omega,ref}}{T_{2\omega,PZA}\,T^2_{\omega,PZA}}} \times \sqrt{\frac{n_{2\omega,PZA}\,n^2_{\omega,PZA}}{n_{2\omega,ref}\,n^2_{\omega,ref}}} \times \sqrt{\frac{K_{2\omega,PZA}}{K_{2\omega,ref}}} \times \left|\frac{J_{2\omega,ref}\left(\Delta k_{ref}\,;z=0..h_{ref}\right)}{J_{2\omega,PZA}\left(\Delta k_{PZA}\,;z=0..h_{PZA}\right)}\right| \times \sqrt{\frac{S^2_{PZA}}{S^2_{ref}}} \times \sqrt{\frac{\alpha_{ref}S_{ref}}{\alpha_{PZA}S_{PZA}}}, \tag{4}$$

where T_ω, $T_{2\omega}$, n_ω, and $n_{2\omega}$ are the Fresnel transmission coefficients and the refractive indices at the fundamental and the second-harmonic frequencies, respectively; where $K_{2\omega}$, $J_{2\omega}(\Delta k; z = 0..h) = \int_0^h \exp(i\Delta k u)/(1 + iu/Z_R)du$ with Z_R the Rayleigh length at 1030 nm, Δk, and S are the measured second-harmonic signal, the second-harmonic effective length,[26] the phase mismatch between the fundamental and the second-harmonic waves, and the laser beam sections at the focal plane, respectively. The *PZA* and *ref* subscripts stand for the silver zinc phosphate glass and the reference sample (i.e., the *BPN* glass), respectively.

After calculations resolving the propagation equations, we estimated the effective second-order nonlinearity in our phosphate glass to be $\chi^{(2)}_{eff} \sim 0.6$ pm V^{-1}, which is typically less than one order of magnitude lower than the reference BPN glass (or typically 1.25 that of a z-cut quartz crystal). By typically considering the third-order response of the phosphate glass to be similar to that of the fused silica,[23] namely $\chi^{(3)} = 2.5 \times 10^{-22}$ V^{2}m^{-2}, we estimated a very strong buried electric field $E_{DC} \sim 0.8 \times 10^9$ V m^{-1}. Frequency conversion thus is rather efficient for such laser-poled micro-structured glasses, opening ways, e.g., for quasi-phase matching applications.

Finally, we demonstrate here the thermal stability of the buried electric field in our tailored phosphate glass. A photoinscribed glass was prepared as described in Sec. II A, and then annealed at several temperatures (30 min for each step from 100 to 400 °C with 50 °C steps) up to glass transition temperature T_g, which is typically 385 °C. After each successive annealing, the sample was reset in our nonlinear microscope and the EFISHG signal was measured as detailed in Sec. III A with the intensity integration of the CCD image, all the experimental parameters being kept the same (probe irradiance and probe polarization, CCD camera settings, and as similar as possible the sample repositioning and the SHG imaging collection).

Figure 7 shows the remarkable stability of the EFISHG signal after the successive thermal treatment from 100 to 350 °C below the glass transition temperature. Such measurements typically show 15%-scale random fluctuations due to the micron-scale dispersion of the sample repositioning, so that the nonlinear voxel was not always exactly positioned the same way with respect to the structures. Such fluctuations are inherent to these measurements since we deal with nontrivial sub-diffraction repositioning of the sample. Nevertheless, these observations evidence that the EFISHG

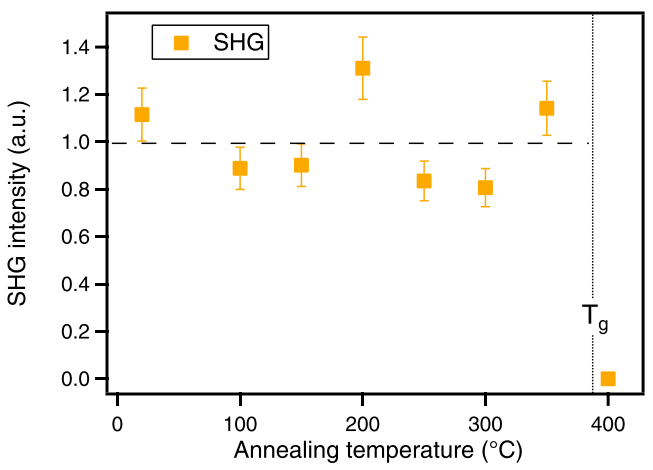

FIG. 7. Integrated EFISHG signal versus annealing temperature applied to the poled structures.

and thus the buried electric field are fully stable under thermal constraint. However, after annealing at 400 °C, that is above the glass transition temperature T_g, the EFISHG signal drastically cancels, down to a null response. This typically results from thermally authorized partial rearrangement of the glass matrix. Above T_g, the buried electric field therefore vanishes, removing the out-of-equilibrium frozen space charge separation. As we observed clearly robust EFISHG signal and buried electric field with temperature, the understanding of such stability is still challenging, since both the origin of mobile charges and their trapping processes are still open questions to investigate.

IV. CONCLUSION AND PERSPECTIVES

In conclusion, we have fabricated efficient EFISHG structures by direct laser poling in a tailored silver-containing phosphate glass. Polarization studies and associated modelling have shown that the laser-induced buried electric field is perpendicular to the linear structures. This buried electric field comes from fs laser-induced permanent space charge separation and stabilization, occurring at the very early stages of the laser-material interaction and resulting in direct laser poling. Such EFISHG behaviour quickly reaches a saturation value, depicting the saturation of the associated DLW-induced space charge separation.

Moreover, coherent imaging microscopy and associated modelling have depicted the spatial EFISHG distribution, corresponding to a non-trivial four-line electric field pattern. Since the width of the EFISHG pattern is typically diffraction-limited by the collection setup, one can expect that the local static electric field distribution is even narrower. The microscopic mechanisms at play for such space charge separation and permanent fixation are still under investigation, taking into account dynamical aspects as well as the role of both existing and generated species as well as the induced local photochemistry.[30,31]

In the considered experimental conditions with the lowest DLW fluencies (3.52 J cm^{-2}), no fluorescence from silver clusters was observed in this tailored silver-containing phosphate glass, proving that the creation of fluorescent silver clusters is not the key process to create the buried space charge separation, but a consequence of it.

Finally, we showed the strong efficiency of the EFISHG structures, as well as the excellent thermal stability of the associated space charge separation under material annealing, since a thermal treatment above the glass transition temperature is required to vanish it. All these features make the DLW-induced EFISHG in our tailored silver-doped phosphate glass a relevant approach for perennial high density data storage or for new nonlinear photonics bricks. Direct laser poling opens experimental access to quasi phase-matched 3D structures in glasses, relevant for parametric frequency conversion interactions for incident light propagating either perpendicular[32] or with any incident angle with respect to the poled domains.[33] This single-beam DLP is especially interesting to design new integrated elements, as functionalized guiding elements (waveguides or fibers), with an enlarged ability to control the spatial patterning of broadband second-order nonlinear properties, compared to that commonly obtained from the two-beam co-illumination.

ACKNOWLEDGMENTS

This work was supported by the French Agency of National Research [ANR 2010 BLAN 94603], the French Aquitaine region [Grant FELINS REGION], and the group of scientific interest GIS-LasINOF.

[1]C. A. Haynam *et al*., Appl. Opt. **46**(16), 3276–3303 (2007).
[2]B. E. A. Saleh and M. C. Teich, *Fundamentals of Photonics* (Wiley, 1991).
[3]J. Extermann, L. Bonacina, F. Courvoisier, D. Kiselev, Y. Mugnier, R. Le Dantec, C. Galez, and J.-P. Wolf, Opt. Express **16**(14), 10405–10411 (2008).
[4]V. M. Shalaev, Nat. Photonics **1**, 41–48 (2007).
[5]P. Pantazis, J. Maloney, D. Wu, and S. E. Fraser, Proc. Natl. Acad. Sci. U.S.A. **107**, 14535–14540 (2010).
[6]K. Miura, J. Qiu, T. Mitsuyu, and K. Hirao, Opt. Lett. **25**, 408–410 (2000).
[7]A. Podlipensky, J. Lange, G. Seifert, H. Graener, and I. Cravetchi, Opt. Lett. **28**, 716 (2003).
[8]R. A. Myers, N. Mukherjee, and S. R. J. Brueck, Opt. Lett. **16**, 1732–1734 (1991).
[9]P. G. Kazansky, L. Dong, and P. St. J. Russell, Opt. Lett. **19**, 701 (1994).
[10]H. Takebe, P. G. Kazansky, and P. St. J. Russel, Opt. Lett. **21**(7), 468–470 (1996).
[11]Y. Quinquempois, N. Godbout, and S. Lacroix, Phys. Rev. A **65**, 043816 (2002).
[12]M. Dussauze, T. Cremoux, G. Yang, F. Adamietz, T. Cardinal, V. Rodriguez, and E. Fargin, Int. J. Appl. Glass Sci. **3**(4), 309–320 (2012).
[13]A. Delestre, M. Lahaye, E. Fargin, M. Bellec, A. Royon, L. Canioni, M. Dussauze, F. Adamietz, and V. Rodriguez, Appl. Phys. Lett. **96**, 091908 (2010).
[14]R. H. Stolen and H. W. K. Tom, Opt. Lett. **12**, 585 (1987).
[15]I. C. S. Carvalho, W. Margulis, and B. Lesche, Opt. Lett. **16**, 1487 (1991).
[16]J. Si, K. Kitaoka, T. Mitsuyu, and K. Hirao, Appl. Phys. Lett. **75**, 307–309 (1999).
[17]J. Qiu, J. Si, and K. Hirao, Opt. Lett. **26**(12), 914–916 (2001).
[18]J. Qiu, M. Shirai, T. Nakaya, J. Si, X. Jiang, C. Zhu, and K. Hirao, Appl. Phys. Lett. **81**, 3040 (2002).
[19]Q.-Z. Zhao, J.-R. Qiu, X.-W. Jiang, C.-J. Zhao, and C.-S. Zhu, Opt. Express **12**, 4035 (2004).
[20]M. Bellec, A. Royon, K. Bourhis, J. Choi, B. Bousquet, M. Treguer, T. Cardinal, J.-J. Videau, M. Richardson, and L. Canioni, J. Phys. Chem. C **114**, 15584–15588 (2010).
[21]L. Canioni, M. Bellec, A. Royon, B. Bousquet, and T. Cardinal, Opt. Lett. **33**, 360–362 (2008).
[22]A. Royon, K. Bourhis, M. Bellec, G. Papon, B. Bousquet, Y. Deshayes, T. Cardinal, and L. Canioni, Adv. Mater. **22**, 5282–5286 (2010).
[23]J. Choi, M. Bellec, A. Royon, K. Bourhis, G. Papon, T. Cardinal, L. Canioni, and M. Richardson, Opt. Lett. **37**, 1029–1031 (2012).
[24]K. Bourhis, A. Royon, M. Bellec, J. Choi, A. Fargues, M. Treguer, J.-J. Videau, D. Talaga, M. Richardson, T. Cardinal, and L. Canioni, J. Non-Cryst. Solids **356**, 2658–2665 (2010).
[25]A. Royon, Y. Petit, G. Papon, M. Richardson, and L. Canioni, Opt. Mater. Express **1**(5), 866–882 (2011).
[26]R. W. Boyd, *Nonlinear Optics* (Academic Press Elsevier, San Diego, 2008).
[27]G. Papon, Y. Petit, N. Marquestaut, A. Royon, M. Dussauze, V. Rodriguez, T. Cardinal, and L. Canioni, Opt. Mater. Express **3**(11), 1855–1861 (2013).
[28]R. Espiau de Lamaestre, H. Béa, H. Bernas, J. Belloni, and J. L. Marignier, Phys. Rev. B **76**, 205431 (2007).
[29]M. Dussauze, E. Fargin, A. Malakho, V. Rodriguez, T. Buveteau, and F. Adamietz, Opt. Mater. **28**, 1417–1422 (2006).
[30]T. G. Alley, S. R. J. Brueck, and R. A. Myers, J. Non-Cryst. Solids **242**, 165–176 (1998).
[31]R. Ascazubi, C. Shneider, I. Wilke, R. Pino, and P. Dutta, Phys. Rev. B **72**, 045328 (2005).
[32]J. Thomas, V. Hilbert, R. Geiss, T. Pertsch, A. Tünnermann, and S. Nolte, Laser Photonics Rev. **7**(3), 17–20 (2013).
[33]Y. Petit, P. Segonds, and B. Boulanger, Phys. Rev. A **76**, 063817 (2007).